RSC Advances

PAPER

View Article Online
View Journal | View Issue

Cite this: *RSC Adv.*, 2015, **5**, 9228

Flexible free-standing 3D porous N-doped graphene–carbon nanotube hybrid paper for high-performance supercapacitors†

Wei Fan,[a] Yue-E Miao,[a] Yunpeng Huang,[a] Weng Weei Tjiu[b] and Tianxi Liu*[a]

Received 3rd November 2014
Accepted 2nd January 2015

DOI: 10.1039/c4ra13675f

www.rsc.org/advances

The nanoarchitecture of carbon with assembled building blocks on diverse scales is of great importance for energy storage. Herein, we demonstrate high-performance supercapacitors by building a three-dimensional (3D) porous structure that consists of a N-doped graphene–carbon nanotube (CNT) hybrid. The 3D porous nitrogen-doped graphene–CNT (p-N-GC) hybrid paper was fabricated by using polystyrene (PS) colloidal particles as a sacrificial template, followed by calcination to remove PS to generate macropores, to reduce graphene oxide (GO) into graphene, and to realize N-doping simultaneously by one step. The as-prepared p-N-GC paper with high porosity, conductivity and flexibility has a high specific capacitance of 294 F g^{-1} at a current density of 1 A g^{-1} in 6 M KOH electrolyte solution, as well as good rate capability and cycle stability. The greatly enhanced electrochemical performance can be ascribed to the synergistic effect of the 3D porous nanostructure, effective CNT intercalation, and nitrogen-doping, suggesting that p-N-GC as novel electrode materials may have potential applications in high-performance energy storage devices.

1. Introduction

Owing to their unique high conductivity and large specific surface area,[1–3] graphene nanosheets are expected to be an ideal material for energy storage and conversion.[4–7] The theoretical specific surface area for completely exfoliated and isolated graphene sheets is ~2600 m^2 g^{-1} and can provide a specific capacitance of about 550 F g^{-1}.[5] However, the irreversible aggregation or restacking of graphene sheets due to the huge interlayer van der Waals attractions has hampered the performance of supercapacitors using graphene materials.[8–10] For instance, graphene-based paper-like materials, which utilize graphene sheets as building blocks in vacuum-assisted self-assembly, have already been developed as binder-free flexible electrodes for supercapacitors due to their excellent mechanical flexibility and electrical conductivity.[11–15] Nevertheless, in most cases, the large specific surface area of the closely-packed and oriented graphene sheets throughout the graphene papers is inevitably lost which significantly reduces their potential application as supercapacitor electrodes.[14,15] Thus, it is still a great challenge to develop a feasible and effective way to fabricate graphene-based hybrid papers as flexible electrodes with relatively high capacitance and without the sacrifice of their good cyclic stability.

Recent reports and reviews have described electrode construction consisting of three-dimensional (3D) interpenetrating structures that could provide a good solution to the issue of poor ionic and electronic transport in electrode materials, thereby resulting in high-performance devices.[16–19] In this regard, graphene has been assembled into various macroscopic 3D porous structures, such as foams,[20] aerogels,[21–23] sponges,[24,25] hydrogels,[26] and networks.[27–30] The 3D porous cross-linked structure of graphene in the above materials can efficiently prevent the face-to-face restacking of graphene. However, the porous material, which is assembled without externally induced orientation, renders a random interconnection structure and exhibits isotropic macroscopic properties. More recently, 3D macroporous graphene structures have been fabricated using graphene oxide (GO) as carbon precursor and polymer as template such as poly(methyl methacrylate) or polystyrene (PS) colloidal particles.[31–34] This template directed method can form much more uniform and controllable porous structures, which can boost ion and electron movement in electrochemical processes. Nevertheless, the templates used are normally in a size from several hundred nanometers to a few micrometers, thus macropores are generated in these structures, which limits the further improvement of the surface area.

Apart from fabricating 3D graphene porous structures, another efficient method to prevent graphene sheets from restacking and further increase the surface area is to introduce

[a]State Key Laboratory of Molecular Engineering of Polymers, Department of Macromolecular Science, Fudan University, 220 Handan Road, Shanghai 200433, P. R. China. E-mail: txliu@fudan.edu.cn; Fax: +86-21-65640293; Tel: +86-21-55664197
[b]Institute of Materials Research and Engineering, A*STAR (Agency for Science, Technology and Research), 3 Research Link, Singapore 117602, Singapore

† Electronic supplementary information (ESI) available. See DOI: 10.1039/c4ra13675f

"spacer" phases (*e.g.* carbon nanotubes (CNTs),[35–38] nanoparticles[39–41] and even "water molecules"[42]) between graphene sheets to form sandwich-type structures. For example, carbon spheres have been attached onto the surface of the graphene sheets and serve as spacers to separate and support the neighboring sheets.[39] Wei *et al.*[35] reported a method to prepare a graphene–CNT hybrid using chemical vapor deposition (CVD) *in situ* growth, and its supercapacitor performance has been studied. A film made from a direct GO–multiwalled CNT mixture has been used for supercapacitors and possesses a specific capacitance of 265 F g^{-1} at 100 mA g^{-1}.[37] Obviously, adding some spacers between the graphene sheets to avoid such restacking and agglomerate formation, is one of effective strategies to materialize the great potential of graphene for supercapacitors, and in the meantime, the spacer could contribute to overall surface area and/or conductivity of the active material.

Although these 3D structures show potential use as capacitive electrodes, those electrical double layer capacitors (EDLCs) exhibit relatively low energy densities due to the intrinsic limitation of the electrostatic surface charging mechanism.[4–6] To address the inferior capacitances of EDLCs, an efficient approach to functionalize and tune the properties of assembled graphene is by the regulation of the carbon–carbon bonds within the planar graphene structures. Recent studies have demonstrated that doping graphene with substituent heteroatoms could effectively modulate the electronic characteristics, surface and local chemical features of graphene, essential for novel device applications.[43,44] For the chemical doping of carbon-based materials, nitrogen (N) is a potential candidate due to its atomic size and strong valence bonds, which are similar to those characteristics of carbon atoms.[45–51] To date, pyrolysis of GO with a low-cost N source, such as urea,[49] melamine,[50] pyrrole[45] and polyaniline (PANI),[51] is a versatile method for large-scale production of N-doped graphene with flexible control over the N-bonding configurations.

In this study, we report a new strategy for the synthesis of 3D porous N-doped graphene–CNT (p-N-GC) hybrid paper, which can be directly used as flexible electrodes possessing both EDL capacitance and pseudocapacitance. This method has at least three advantages over traditional methods reported in the literature: (1) compared with bare graphene paper, graphene–CNT hybrid papers exhibit much higher porosity and improved electrical conductivities by using CNTs as both the spacers and conductive linkers between individual graphene sheets; (2) 3D porous nanostructure greatly enhances the specific surface area, improving both ionic and electronic transport kinetics; (3) the effective N-doping of graphene can increase electron mobility and space charge capacitance, thus further enhance the pseudocapacitance. This provides a green way for controllable and regular graphene film for binder-free supercapacitor electrode with high rate capability, mechanical flexibility and enhanced gravimetric capacitance.

2. Experimental section

2.1 Materials

Natural graphite powder (325 meshes) was purchased from Alfa-Aesar. Multiwalled carbon nanotubes (length, 10–30 μm; outer diameter, 40–50 nm; purity, 95%), produced by the CVD method, were supplied by Chengdu Institute of Organic Chemistry, Chinese Academy of Sciences, China. Aniline and styrene were purchased from Sigma-Aldrich. Potassium persulfate (KPS), ammonium persulfate (APS), ethanol, 98% H_2SO_4, 30% H_2O_2, $KMnO_4$, $NaNO_3$ and 37% HCl were supplied by China Medicine Co. Aniline and styrene were purified by distillation, and other reagents were used as received without further treatment. Deionized (DI) water was used throughout all the experiments.

2.2 Preparation of PS@PANI and aqueous suspension of GO–CNT hybrid

Monodispersed PS spheres with diameters of 270 nm were synthesized according to the procedures reported elsewhere.[52] Then, the as-prepared PS spheres were dispersed in concentrated sulfuric acid, and the sulfonation reaction was allowed to take place at 40 °C for 6 h under stirring. After centrifugation and washing processes, sulfonated PS was obtained and then dispersed in 30 mL of DI water. Subsequently, a certain amount of aniline monomer in 1 M HCl solution was added to the above solution under stirring in an ice bath. An aqueous solution of APS (1 : 1 molar ratio of APS to aniline) was added, and the reaction was allowed to proceed for 24 h at 0 °C. The PS@PANI spheres were collected by repeatedly centrifuging and washing with ethanol and water, respectively. Stable aqueous solutions of GO–CNT hybrid were prepared by our method reported previously.[53,54] Briefly, graphite oxide was synthesized by Hummers method,[55] and exfoliated to give a brown dispersion of GO (1.0 mg mL^{-1}) under ultrasonication. The aqueous colloidal suspensions of GO sheets were then mixed with different amount of CNT conglomerations, and the mixture was then sonicated for 1 h at 45 W. This suspension was centrifuged for 30 min at 8000 rpm to remove the unstabilized CNTs, thus giving a stable suspension of the GO–CNT hybrids.

2.3 Fabrication of porous N-doped graphene–CNT hybrid paper

A designed amount of PS@PANI suspension (0.5 mg mL^{-1}) was added to GO–CNT suspension drop by drop, and the resulting mixture was sonicated for another 2 h. Subsequently, the mixed suspension containing PS@PANI spheres and GO–CNT hybrids was vacuum-filtrated through a poly(vinylidene fluoride) (PVDF) membrane filter (220 nm pore size, Durapore® from Sigma-Aldrich). To obtain a free-standing hybrid paper, the paper was dried at room temperature, and then carefully peeled off from the membrane filter. Subsequently, the as-prepared GO–CNT/PS@PANI hybrid paper was placed in an alumina crucible and calcinated in a horizontal furnace under pure nitrogen gas atmosphere at 800 °C with a heating rate of 5 °C min^{-1}, and left for 4 h at the final temperature. The obtained p-N-GC hybrid

paper with GO to CNT weight ratios of 2/1, 1/1 and 1/2 were denoted as p-N-G2C1, p-N-G1C1, and p-N-G1C2, respectively. For comparison, porous nitrogen-doped graphene (p-N-graphene) paper, neat graphene–CNT hybrid (G1C1) paper and porous graphene–CNT hybrid (p-G1C1) paper were also fabricated in a similar way without adding CNT or PS@PANI or PANI.

2.4 Characterization

Transmission electron microscopy (TEM) observation was performed with a JEOL 2100 TEM under an accelerating voltage of 200 kV. Field emission scanning electron microscopy (FESEM) characterization was conducted with a JSM-6700F SEM at an accelerating voltage of 5 kV. The surface charge of synthesized PS@PANI and GO–CNT hybrids was measured using a ζ-potential analyzer (Malvern, Zetasizer nanozs). The Brunauer–Emmett–Teller (BET) surface area was measured using a Belsorp-max surface area detecting instrument by N_2 physisorption at 77 K. X-ray photoelectron spectroscopy (XPS) spectra were measured using a Phoibos 100 spectrometer with a monochromatic Mg X-ray radiation source. All XPS spectra were fit using XPS Peak 4.1 software.

2.5 Electrochemical measurements

The electrochemical tests were carried out in 6 M KOH electrolyte solution by a two-electrode system. Ni foams were used as current collector and filter paper served as a separator. The as-prepared hybrid papers were cut into 10 mm × 10 mm square and used directly as the binder-free electrode material. The mass loading of a single electrode is about 1.2 mg. Cyclic voltammetry (CV), galvanostatic charge/discharge curves and electrochemical impedance spectroscopy (EIS) were performed with a CHI 660C electrochemical workstation (Chenhua Instruments Co., Shanghai, China). CV curves were collected at different scan rates in a range from −0.6 to 0.4 V and galvanostatic charge/discharge curves were measured in a voltage ranging from −0.6 to 0.4 V. EIS was recorded in the frequency range from 10^5 to 0.01 Hz at open circuit potential with an AC voltage amplitude of 5 mV.

The specific capacitance C_s (F g^{-1}) of the samples was estimated from the discharge process according to the following equation:

$$C_s = \frac{4I\Delta t}{\Delta V \times m} \quad (1)$$

where I is the current loaded (A), Δt is the discharge time (s), ΔV is the potential change during discharge process, and m is the total mass of the two electrodes (g).

3. Results and discussion

Fig. 1a shows the SEM images of PS@PANI spheres. Aniline can be adsorbed on the surface of sulfonated PS spheres and further *in situ* polymerized on the PS sphere surface when the oxidant is added, resulting in the formation of PS@PANI spheres. It was observed that these PS@PANI spheres were uniform in size with

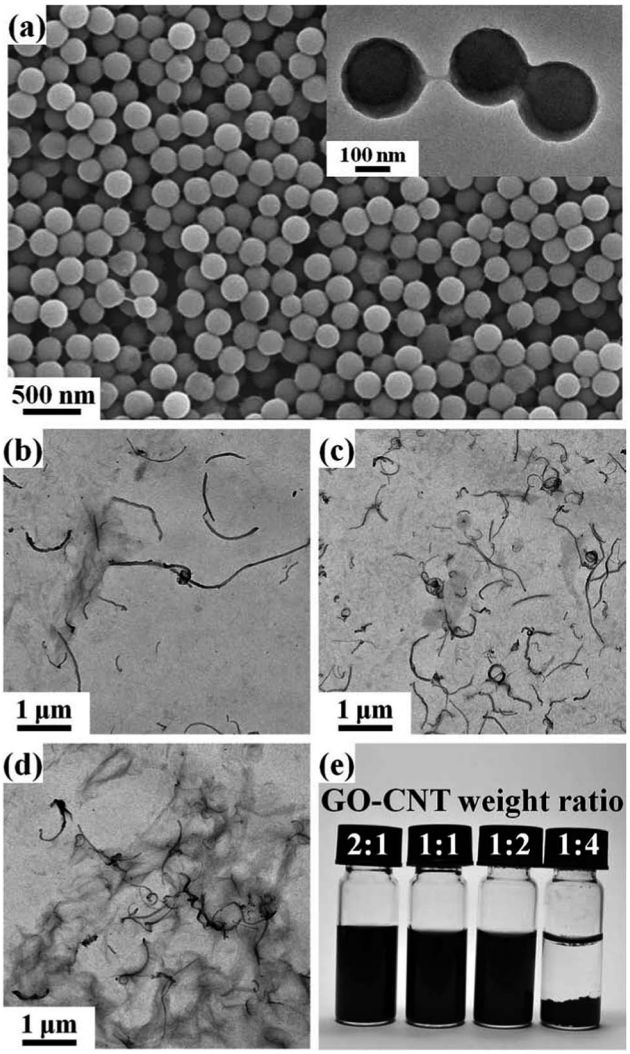

Fig. 1 (a) SEM images of PS@PANI. Inset shows the corresponding TEM image. TEM images of GO–CNT hybrids with weight ratios of (b) 2 : 1, (c) 1 : 1, and (d) 1 : 2. (e) Digital photos showing GO–CNT suspensions with different weight ratio after settling for one month.

an average diameter of 300 nm. From the inset TEM image, the clear core–shell structure can be observed with an average thickness of the PANI layer estimated to be about 20 nm. Using the same procedures as in our previous studies on assisted dispersion of CNTs using GO sheets as versatile dispersants in aqueous media, homogeneous aqueous dispersions of GO–CNT hybrids were prepared with varied weight ratios. The proportions of GO to pristine CNTs were adjusted by producing GO sheet dispersions with a concentration of 1.0 mg mL^{-1} and controlling the added amount of pristine CNTs. It was found that a series of stable black dispersions can be obtained with the weight ratio of GO to CNTs larger than 1/2, indicating strong stabilizing ability of the GO sheets for the pristine CNTs in water. It is reasonable to suppose that the π-conjugated multiple aromatic regions of GO sheets could interact with the sidewalls of CNTs through the π–π stacking interaction, while the hydrophilic oxygen groups maintain the water solubility of

the GO–CNT complexes. Adding a larger amount of pristine CNTs to the GO suspension will cause the co-precipitation of GO and CNTs. The formation of GO–CNT hybrids can be strongly supported by morphological observations. As shown in Fig. 1b–c, hair-like CNTs were randomly adsorbed on the smooth surface of the GO sheets, and no individual GO sheets or CNTs were found in the view. This phenomenon clearly indicates strong interactions between the two kinds of nano-elements during the formation of GO–CNT hybrids. With increasing the amount of CNTs, more CNTs were attached or adsorbed on the GO sheets (from Fig. 1b–c). Although GO–CNT hybrids with a weight ratio of 1/2 can still form a stable suspension, some twisted CNTs can be observed on GO sheets, indicating a reduced solubility. The aqueous dispersion of GO–CNT hybrids with different weight ratios was assessed by sedimentation experiments, as shown in Fig. 1e.

The 3D p-N-GC hybrid paper was prepared in two steps: fabrication of free-standing GO–CNT/PS@PANI hybrid paper by vacuum filtration of a mixed aqueous colloidal suspension of GO–CNT hybrids and PS@PANI nanospheres, followed by calcination to remove the PS to generate 3D macropores, to reduce GO into graphene, and to pyrolyze PANI realizing N-doping (Scheme 1). This filtration process is suitable for macroscopic assembly of GO sheets into paper-like bulk materials with lightweight and mechanical flexibility.[11] Well-ordered free-standing GO–CNT/PS@PANI hybrid paper was fabricated by first separately preparing a negatively charged GO–CNT colloid and a positively charged PS@PANI suspension, followed by filtration. The GO–CNT suspension was intrinsically negatively charged due to the introduction of functional groups such as carboxylic acids (–COOH) on the surface of graphene sheets, while the as-formed PS@PANI was proved to be positively charged in their emeraldine salt form. As determined by ζ-potential measurements, the ζ-potential values of the two dispersions are −50 mV for GO–CNT hybrids and +23 mV for PS@PANI, respectively. Through a filtration process, GO–CNT hybrids and PS@PANI were assembled due to the electrostatic interactions and hydrophobic characteristics between them, and subsequently integrated into GO–CNT/PS@PANI hybrid paper. SEM images of the cross-section of the GO–CNT/PS@PANI hybrid paper clearly show that GO–CNT embedded with PS@PANI nanospheres were packed into multilayers, forming crinkles and rough textures (Fig. S1†). PS@PANI nanospheres and CNTs were evenly embedded between the inter-layers of GO sheets, indicating a good dispersibility. Moreover, it is noteworthy that the dimensions of PS spheres (~300 nm) as well as the intrinsic flexibility of graphene are appropriate enough to hold the curvature and thus the overall porous structure.

The as-prepared GO–CNT/PS@PANI hybrid paper was then calcinated under nitrogen atmosphere to remove the PS nanospheres. At the same time, GO was thermally reduced and PANI was carbonized to form N-doped graphene. Thus, 3D porous N-doped graphene–CNT hybrid paper was prepared. As shown by the digital photos in Scheme 1, the free-standing hybrid paper has good flexibility which can be bent and held by a tweezer. SEM images of both the surface and cross-section of the p-N-GC hybrid papers with different graphene to CNT ratios are shown in Fig. S2† and 2, respectively. As shown in Fig. S2,† with the increase of CNT content, the roughness and porosity of the surface of the paper increases obviously, which is mainly due to that CNTs can act as spacers preventing graphene sheets from restacking. Fig. 2 shows the fractured edges of p-N-GC hybrid papers with different graphene to CNT ratios. The thickness of these papers was approximately 8 μm, and all the hybrid papers clearly exhibit a well-packed layered structure through the entire cross-sections, indicating that graphene–CNT hybrids can be assembled to form parallel arranged nanostructures under filtration-induced directional flow. CNTs are incorporated between large lateral dimensional graphene layers, resulting in sandwiched structures. And there are uniform pores evenly distributed between the parallel arranged graphene–CNT frameworks, resulting from the removal of PS templates which leaves behind an open porous structure. This porous structure cannot be observed when the PS@PANI nanospheres are not added, as shown in Fig. S3a and b.† The

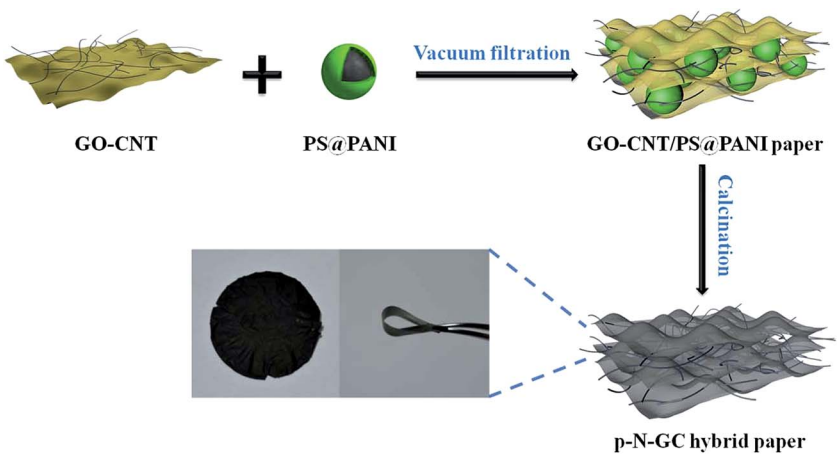

Scheme 1 Schematic illustration for the preparation of 3D porous N-doped graphene–CNT hybrid paper. Digital photos of the free-standing p-N-G1C1 paper peeled off from the filter membrane and held by a tweezer, showing good flexibility.

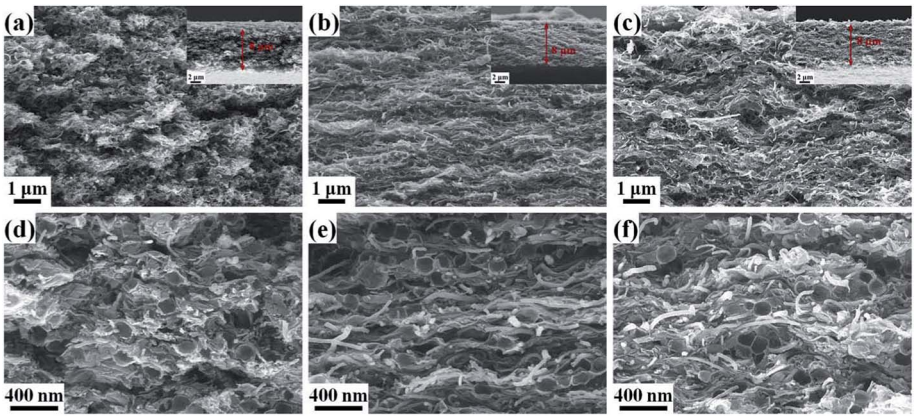

Fig. 2 Cross-section SEM images of (a and d) p-N-G2C1, (b and e) p-N-G1C1, and (c and f) p-N-G1C2 at (a–c) low and (d–f) high magnifications, respectively. Insets show the corresponding SEM images at low magnification, indicating the thickness of the paper.

porous structure did not collapse and thus duplicate the original template structure very well because of the interconnected nature of the multilayered graphene walls in the assembled 3D structure. The mechanical strength of graphene, the pore size, and thermal stability synergistically help preserve the porous structure even after calcination. However, it is noteworthy that without CNTs, the porous graphene paper has a much more compact layered structure as shown in Fig. S3c and d.† Here, CNTs can act as both the spacers and conductive linkers between individual graphene sheets, which can destroy the well-ordered structure of layered graphene, thus contributing to higher porosity and conductivity.

The porous structure of p-N-GC hybrid paper is also confirmed by TEM images. Fig. 3a and b clearly show a porous structure throughout the entire sample, which is consistent with the SEM observations. The porous structure and the flat layer as well as CNTs can be clearly observed, suggesting that the foam-like structure is constructed by graphene sheets and CNTs. In particular, energy-dispersive X-ray spectroscopic (EDS) elemental maps of C, O, and N (Fig. 3c) clearly verified the homogeneous doping of nitrogen heteroatoms throughout the 3D nanoporous frameworks.

The successful doping (elemental compositions and heteroatom bonding configurations) of graphene with N atoms is further investigated using XPS spectra. As shown in Fig. 4a, p-N-G1C1 sample has a predominant graphitic C1s peak at about 284.8 eV, a weak O1s peak at 532.0 eV, and a pronounced N1s peak located at 400.0 eV, without any evidence of impurities, verifying the doping of N-atoms within p-N-G1C1. The nitrogen

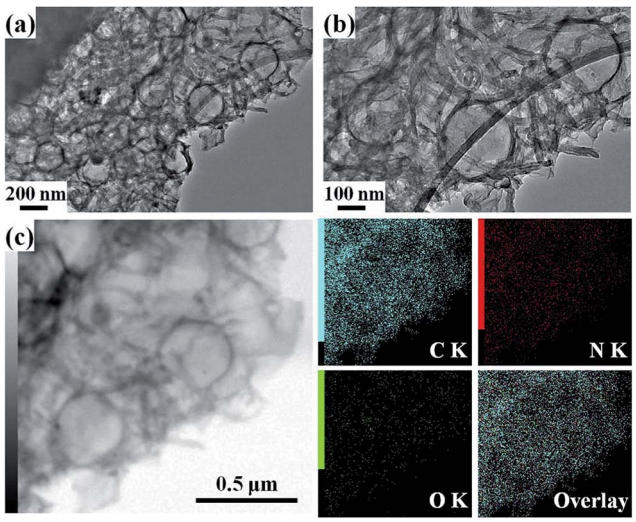

Fig. 3 TEM images of p-N-G1C1 at (a) low and (b) high magnifications. (c) EDS mapping of C, O, N, and overlay elements on a segment of p-N-G1C1 paper.

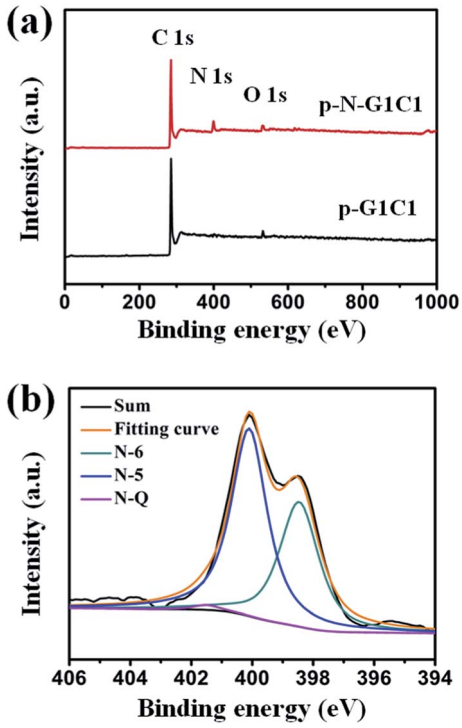

Fig. 4 (a) XPS spectra of p-G1C1 and p-N-G1C1. (b) N1s spectra of p-N-G1C1.

atomic content of p-N-G1C1 sample is found to be 8.4%. The high resolution N1s spectrum was used primarily to determine the bonding configurations of N-atoms in p-N-G1C1. As shown in Fig. 4b, the peak deconvolution suggests three components in p-N-G1C1 sample centered at 398.5, 400.1, and 401.5 eV, corresponding to pyridinic-*N* (*N*-6), pyrrolic-*N* (*N*-5), and quaternary-*N* (*N*-Q), respectively.[51] The percentages of *N*-6, *N*-5 and *N*-Q are estimated to be 45.9%, 50.6%, and 3.5%, respectively. As reported previously, the presence of pyridinic and pyrrolic forms of nitrogen in graphene is favorable for the enhancement of electrochemical performance of the materials.[46] The pyridinic nitrogen, which can provide a lone electron pair for conjugation with the π-conjugated rings, is electrochemically active nitrogen. Pyrrolic nitrogen, which improves the charge mobility in a carbon matrix by introducing electron-donor characteristics and enhancing the carbon catalytic activity in electron-transfer reactions, is also electrochemically active nitrogen.[56] Therefore, the pseudocapacitance is mainly induced by pyridinic and pyrrolic nitrogen.

BET specific surface area of the p-N-graphene and p-N-G1C1papers were further investigated by nitrogen isothermal adsorption, as shown in Fig. 5. The isotherm curves show a type IV isotherm with a steep increase of nitrogen absorption at a high relative pressure (P/P_0 = 0.80–0.99), indicating that the main pore volume is contributed by large size pores. The specific surface area of p-N-graphene and p-N-G1C1 are 350 and 651 $m^2\ g^{-1}$, respectively, significantly larger than the values of the dried graphene (44 $m^2\ g^{-1}$),[57] suggesting that the introduction of PS nanoparticles between 2D graphene sheets efficiently limits the face-to-face stacking between graphene layers. Furthermore, p-N-G1C1 paper has a much larger surface area as compared with p-N-graphene, which is possibly due to the existence of CNTs in this 3D hierarchical structure acting as spacers to completely prevent graphene sheets from restacking. The inset in Fig. 5 shows the pore size distribution of p-N-G1C1 sample obtained by the Barrett–Joiner–Halenda (BJH) method. The majority pore sizes are narrowly distributed at about 3 nm, which is in the mesoporous range, indicating that mesopores can be generated by CNT spacers. Therefore, the CNTs can act as spacers which can completely prevent graphene sheets from restacking, resulting in a largely improved surface area.

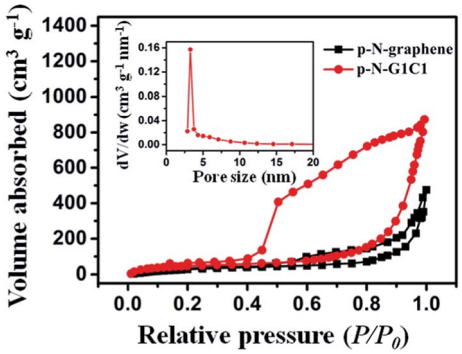

Fig. 5 Nitrogen sorption isotherms of p-N-graphene and p-N-G1C1. The inset shows the corresponding pore size distribution of p-N-G1C1 paper.

The as-obtained p-N-GC hybrid paper with novel porous structure and excellent electrical conductivity are promising candidates for a high rate supercapacitor electrode. The capacitive performance of p-N-GC hybrid paper was evaluated *via* a two-electrode system method in 6 M KOH aqueous electrolyte, as shown in Fig. 6a. Fig. 6b illustrates the CV curves of G1C1, p-G1C1, p-N-G2C1, p-N-G1C1, and p-N-G1C2 papers at a scan rate of 10 mV s^{-1}. The curves of all the samples exhibit an approximately rectangular shape with a small hump, indicating a small pseudo-capacitance in addition to the EDL capacitance, which would be caused by the chemical state of nitrogen in graphene sheets. The difference in the relative specific capacitance can be evaluated by comparing the area under the CV curve within the potential window.[5] The area under the CV curve of p-N-G1C1 is greater than those of the other samples, indicating that the specific capacitance of p-N-G1C1 is the highest among the samples. The capacitance of all the three p-N-GC papers is much higher than those of pure G1C1 paper without macropores and N-doping, and p-G1C1 without N-doping, indicating the positive effect of the 3D porous nanostructure and N-doping. The 3D porous nanostructure greatly enhances the specific surface areas, providing short transport lengths for both mass and charge transport and decreased diffusion resistance of electrolyte ions in the electrode. The insertion of N-atoms into graphene layers can change values of HOMO and LUMO in order to reduce the band gap, thus increase electron mobility and lower the electron work function at the carbon/liquid interface in comparison to pure carbon.[58,59] Therefore, 3D porous nanostructure and high N-doping level are two important factors for obtaining a high specific capacitance.

Moreover, it is noteworthy that the p-N-graphene paper without CNTs has a much lower capacitance as compared to those p-N-GC hybrid papers (Fig. S4†). Due to the existence of CNTs in this 3D hierarchical structure, graphene sheets could be kept completely from restacking if the initial homogeneous distribution of CNTs and graphene sheets is completely kept. It should be noted that, in this ideal state, the entire surface of graphene could be exposed, and the electrolyte ions would also use the channels generated by the CNT spacer and thus facilitate the charging/recharging process of the devices.[60] Furthermore, the weight ratio of graphene to CNTs of p-N-GC hybrid papers also has a great effect on the capacitor performance. From the CV curves shown in Fig. 6b, the capacitance of p-N-G1C1 is higher than the other two counterparts, p-N-G2C1 and p-N-G1C2. Possible explanation is illustrated in Scheme 2. As shown in Scheme 2, we can see that when the ratio of graphene to CNTs increases such as from part b to part a in Scheme 2, the restacking of graphene will be serious. This could have an influence on the effective surface area of the graphene material, and thus the effective contribution of graphene to the overall capacitance of the entire electrode active material would decrease. On the contrary, when decreasing the ratio of graphene to CNTs to 1/2, a small amount of CNTs would aggregate between graphene inter-layers (part c in Scheme 2), which is consistent with the TEM image shown in Fig. 1d. Therefore, the

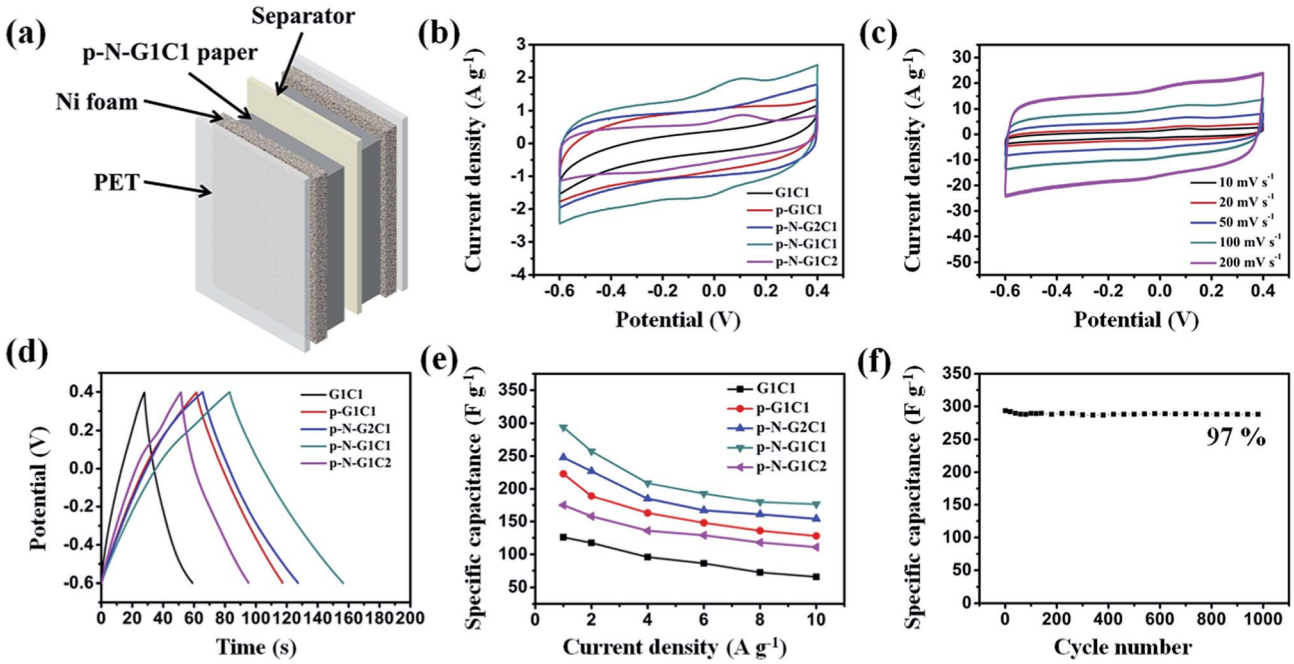

Fig. 6 (a) Schematic diagram of p-N-GC paper based supercapacitor device. (b) CV curves of G1C1, p-G1C1, p-N-G2C1, p-N-G1C1, and p-N-G1C2 papers at a scan rate of 10 mV s^{-1} in 6 M KOH solution. (c) CV curves of p-N-G1C1 paper at different scan rates of 10, 20, 50, 100, and 200 mV s^{-1}, respectively. (d) Galvanostatic charge/discharge curves of G1C1, p-G1C1, p-N-G2C1, p-N-G1C1, and p-N-G1C2 paper within a potential window of −0.6–0.4 V at a current density of 1 A g^{-1}. (e) Plots of specific capacitance for G1C1, p-G1C1, p-N-G2C1, p-N-G1C1, and p-N-G1C2 papers at various current densities. (f) Cycling stability of p-N-G1C1 paper upon charging/discharging at a current density of 1 A g^{-1}.

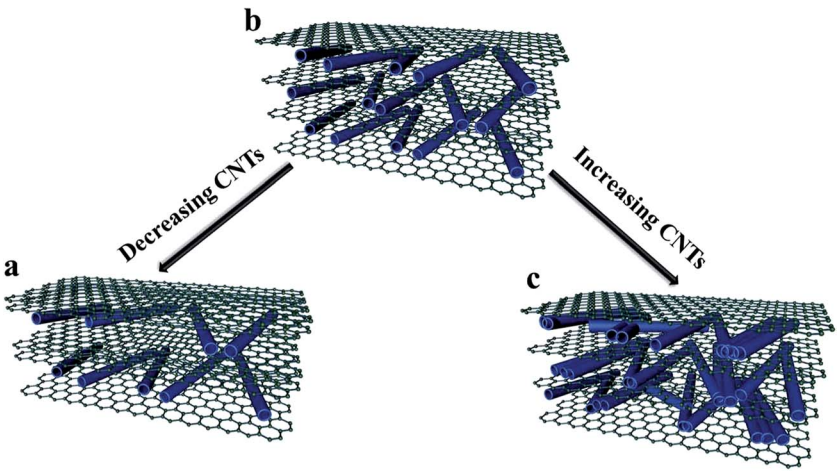

Scheme 2 Schematic diagram of graphene–CNT hybrid structure engineering with different spacer CNT loadings.

loading ratio of CNTs could engineer the hybrid structure and the overall capacitance of the graphene–CNT hybrids. Fig. 6c shows the CV curves of p-N-G1C1 paper at different scan rates. It is notable that the synthesized materials exhibit excellent electrochemical behavior in a wide range of scan rates. In addition, the obvious increase of average current density with the scan rates indicates good rate ability for the p-N-G1C1 electrode.

The representative charge/discharge curves at a current density of 1 A g^{-1} are shown in Fig. 6d. The charge/discharge curve of p-N-GC paper is not a perfect symmetric triangle feature, indicating a major pseudo-capacitive contribution of the surface functionalities in addition to the EDL capacitance. And no obvious potential drop (*IR* drop) is observed, indicating a low internal resistance which is of great importance in energy storage devices, since less energy will be wasted to produce unwanted heat during charge/discharge processes.[13] Specific capacitances estimated from the discharge process at a current density of 1 A g^{-1} of G1C1, p-G1C1, p-N-G2C1, p-N-G1C1, and p-N-G1C2 papers were 126, 223, 248, 294, and 175 F g^{-1}, respectively. The capacitance of p-N-G1C1 paper is obviously higher

than those reported for pure graphene–CNT hybrid based electrodes which can only reach an EDL capacitance of less than 200 F g^{-1}.[36,37,61] The p-N-G1C1 paper provides a novel electrode material advantageously combining the unique porous nanostructure which maximizes the exposure of their surfaces to electrolyte with effective N-doping to further enhance the capacitance by introducing pseudocapacitance. The specific capacitances of the prepared electrode materials as a function of current densities were shown in Fig. 6e. Obviously, the p-N-G1C1 hybrid paper has the highest specific capacitance among all the samples at a wide range of current densities. Even at the high current density of 10 A g^{-1}, the capacitance of p-N-G1C1 paper still reaches 176 F g^{-1}, indicating a better sustainability to high current and an improved rate performance.

Cycling performance is another key factor in determining the supercapacitor electrodes for many practical applications. The cycling tests for p-N-G1C1 paper were carried out under the same current density of 1 A g^{-1}, as shown in Fig. 6f. It is shown that the specific capacitance of the as-made electrodes decreases only by less than 3% after 1000 charge/discharge cycles, demonstrating the good cyclic stability of the hybrid paper as a flexible electrode material.

Further understanding of the fast ion diffusion in porous hybrid films was obtained by conducting impedance measurements at a frequency range of 100 kHz to 0.01 Hz. The Nyquist plots of G1C1, p-G1C1, and p-N-G1C1 papers are displayed in Fig. 7. The intersection of the curves at the real axis in the range of high-frequency represents solution resistance (R_s).[6] The R_s values of p-G1C1 and p-N-G1C1 papers are lower than that of G1C1 (non-porous counterparts), which should be associated with the increased contact area at the electrode/electrolyte interface. Again, the porous nature of the p-N-G1C1 samples plays a critical role. At the low frequency region, a more vertical straight line was evident for p-N-G1C1 paper than for p-G1C1 one, showing a better capacitor behavior. This result clearly implies that the electrolyte ions move more easily into the 3D porous channels compared to the 2D packed structure and the effective N-doping further increases the electron mobility.

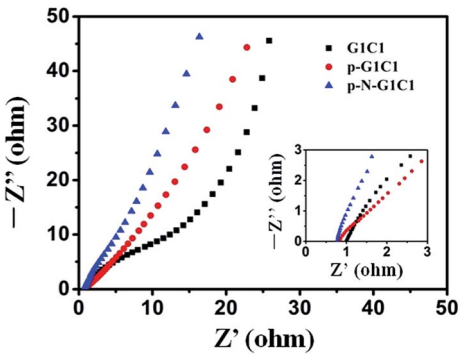

Fig. 7 Nyquist plots for G1C1, p-G1C1, and p-N-G1C1 papers. Z': real impedance. Z'': imaginary impedance. Inset shows an enlarged scale.

4. Conclusions

In conclusion, 3D porous N-doped graphene–CNT hybrid paper, was obtained by a facile hard-template-directed assembly approach. The GO precursor and PS@PANI sphere template were orderly assembled by vacuum filtration, followed by calcination to reduce GO into graphene, to remove the template, as well as to realize N-doping *via* pyrolysis. The 3D porous nanostructure provides rapid pathways for ionic and electronic transport, CNTs act as both the spacers and conductive linkers between individual graphene sheets, and N-doping further increases the electron mobility, thus providing tremendous potential for energy storage applications. Based on the synergistic function of 3D porous nanostructure, effective CNT intercalation and N-doping, the free-standing p-N-GC paper based binder-free supercapacitor device enabled the combination of high capacitance, high rate capability, and long cycling life. Therefore, this work provides a simple and green synthetic strategy to obtain free-standing porous graphene–CNT assemblies with tunable nanostructures, which shows promising prospects towards other applications in biology, energy conversion and catalysis.

Acknowledgements

The authors are grateful for the financial support from the National Natural Science Foundation of China (51125011, 51433001).

Notes and references

1 A. K. Geim and K. S. Novoselov, *Nat. Mater.*, 2007, **6**, 183–191.
2 K. S. Novoselov, A. K. Geim, S. V. Morozov, D. Jiang, M. I. Katsnelson, I. V. Grigorieva, S. V. Dubonos and A. A. Firsov, *Nature*, 2005, **438**, 197–200.
3 K. S. Novoselov, A. K. Geim, S. V. Morozov, D. Jiang, Y. Zhang, S. V. Dubonos, I. V. Grigorieva and A. A. Firsov, *Science*, 2004, **306**, 666–669.
4 M. D. Stoller, S. J. Park, Y. W. Zhu, J. H. An and R. S. Ruoff, *Nano Lett.*, 2008, **8**, 3498–3502.
5 C. G. Liu, Z. N. Yu, D. Neff, A. Zhamu and B. Z. Jang, *Nano Lett.*, 2010, **10**, 4863–4868.
6 Y. Wang, Z. Q. Shi, Y. Huang, Y. F. Ma, C. Y. Wang, M. M. Chen and Y. S. Chen, *J. Phys. Chem. C*, 2009, **113**, 13103–13107.
7 Y. Huang, J. Liang and Y. Chen, *Small*, 2012, **8**, 1805–1834.
8 C. K. Chua and M. Pumera, *Chem. Soc. Rev.*, 2014, **43**, 291–312.
9 D. R. Dreyer, S. Park, C. W. Bielawski and R. S. Ruoff, *Chem. Soc. Rev.*, 2010, **39**, 228–240.
10 S. Eigler and A. Hirsch, *Angew. Chem., Int. Ed.*, 2014, **53**, 7720–7738.
11 D. A. Dikin, S. Stankovich, E. J. Zimney, R. D. Piner, G. Dommett, G. Evmenenko, S. T. Nguyen and R. S. Ruoff, *Nature*, 2007, **448**, 457–460.

12 D. W. Wang, F. Li, J. P. Zhao, W. C. Ren, Z. G. Chen, J. Tan, Z. S. Wu, I. Gentle, G. Q. Lu and H. M. Cheng, *ACS Nano*, 2009, **3**, 1745–1752.
13 Q. Wu, Y. X. Xu, Z. Y. Yao, A. R. Liu and G. Q. Shi, *ACS Nano*, 2010, **4**, 1963–1970.
14 S. L. Zhang, Y. M. Li and N. Pan, *J. Power Sources*, 2012, **206**, 476–482.
15 F. Liu, S. Y. Song, D. F. Xue and H. J. Zhang, *Adv. Mater.*, 2012, **24**, 1089–1094.
16 S. Nardecchia, D. Carriazo, M. L. Ferrer, M. C. Gutierrez and F. Del Monte, *Chem. Soc. Rev.*, 2013, **42**, 794–830.
17 S. Y. Yin, Z. Q. Niu and X. D. Chen, *Small*, 2012, **8**, 2458–2463.
18 S. Chabi, C. Peng, D. Hu and Y. Q. Zhu, *Adv. Mater.*, 2014, **26**, 2440–2445.
19 L. L. Jiang and Z. J. Fan, *Nanoscale*, 2014, **6**, 1922–1945.
20 Z. Q. Niu, J. Chen, H. H. Hng, J. Ma and X. D. Chen, *Adv. Mater.*, 2012, **24**, 4144–4150.
21 H. Y. Sun, Z. Xu and C. Gao, *Adv. Mater.*, 2013, **25**, 2554–2560.
22 Z. Xu, Y. Zhang, P. G. Li and C. Gao, *ACS Nano*, 2012, **6**, 7103–7113.
23 H. Hu, Z. B. Zhao, W. B. Wan, Y. Gogotsi and J. S. Qiu, *Adv. Mater.*, 2013, **25**, 2219–2223.
24 C. H. Wang, X. D. He, Y. Y. Shang, Q. Y. Peng, Y. Y. Qin, E. Z. Shi, Y. B. Yang, S. T. Wu, W. J. Xu, S. Y. Du, A. Y. Cao and Y. B. Li, *J. Mater. Chem. A*, 2014, **2**, 14994–15000.
25 F. Liu and T. S. Seo, *Adv. Funct. Mater.*, 2010, **20**, 1930–1936.
26 Y. X. Xu, K. X. Sheng, C. Li and G. Q. Shi, *ACS Nano*, 2010, **4**, 4324–4330.
27 B. Tang, G. X. Hu, H. Y. Gao and Z. X. Shi, *J. Power Sources*, 2013, **234**, 60–68.
28 J. J. Liu, W. Lv, W. Wei, C. Zhang, Z. J. Li, B. H. Li, F. Y. Kang and Q. H. Yang, *J. Mater. Chem. A*, 2014, **2**, 3031–3037.
29 Z. P. Chen, W. C. Ren, L. B. Gao, B. L. Liu, S. F. Pei and H. M. Cheng, *Nat. Mater.*, 2011, **10**, 424–428.
30 Z. S. Wu, Y. Sun, Y. Z. Tan, S. B. Yang, X. L. Feng and K. Mullen, *J. Am. Chem. Soc.*, 2012, **134**, 19532–19535.
31 B. G. Choi, M. Yang, W. H. Hong, J. W. Choi and Y. S. Huh, *ACS Nano*, 2012, **6**, 4020–4028.
32 C. M. Chen, Q. Zhang, C. H. Huang, X. C. Zhao, B. S. Zhang, Q. Q. Kong, M. Z. Wang, Y. G. Yang, R. Cai and D. S. Su, *Chem. Commun.*, 2012, **48**, 7149–7151.
33 Z. L. Wang, D. Xu, H. G. Wang, Z. Wu and X. B. Zhang, *ACS Nano*, 2013, **7**, 2422–2430.
34 X. D. Huang, K. Qian, J. Yang, J. Zhang, L. Li, C. Z. Yu and D. Y. Zhao, *Adv. Mater.*, 2012, **24**, 4419–4423.
35 Z. J. Fan, J. Yan, L. J. Zhi, Q. Zhang, T. Wei, J. Feng, M. L. Zhang, W. Z. Qian and F. Wei, *Adv. Mater.*, 2010, **22**, 3723–3728.
36 N. Jha, P. Ramesh, E. Bekyarova, M. E. Itkis and R. C. Haddon, *Adv. Energy Mater.*, 2012, **2**, 438–444.
37 X. J. Lu, H. Dou, B. Gao, C. Z. Yuan, S. D. Yang, L. Hao, L. F. Shen and X. G. Zhang, *Electrochim. Acta*, 2011, **56**, 5115–5121.
38 X. C. Dong, Y. W. Ma, G. Y. Zhu, Y. X. Huang, J. Wang, M. B. Chan-Park, L. H. Wang, W. Huang and P. Chen, *J. Mater. Chem.*, 2012, **22**, 17044–17048.
39 C. X. Guo and C. M. Li, *Energy Environ. Sci.*, 2011, **4**, 4504–4507.
40 H. L. Wang, L. F. Cui, Y. A. Yang, H. S. Casalongue, J. T. Robinson, Y. Y. Liang, Y. Cui and H. J. Dai, *J. Am. Chem. Soc.*, 2010, **132**, 13978–13980.
41 H. L. Wang, H. S. Casalongue, Y. Y. Liang and H. J. Dai, *J. Am. Chem. Soc.*, 2010, **132**, 7472–7477.
42 X. W. Yang, J. W. Zhu, L. Qiu and D. Li, *Adv. Mater.*, 2011, **23**, 2833–2838.
43 Q. Tang, Z. Zhou and Z. F. Chen, *Nanoscale*, 2013, **5**, 4541–4583.
44 Z. Liu, H. G. Nie, Z. Yang, J. Zhang, Z. P. Jin, Y. Q. Lu, Z. B. Xiao and S. M. Huang, *Nanoscale*, 2013, **5**, 3283–3288.
45 Y. Zhao, C. G. Hu, Y. Hu, H. H. Cheng, G. Q. Shi and L. T. Qu, *Angew. Chem., Int. Ed.*, 2012, **51**, 11371–11375.
46 H. M. Jeong, J. W. Lee, W. H. Shin, Y. J. Choi, H. J. Shin, J. K. Kang and J. W. Choi, *Nano Lett.*, 2011, **11**, 2472–2477.
47 Y. H. Xue, J. Liu, H. Chen, R. G. Wang, D. Q. Li, J. Qu and L. M. Dai, *Angew. Chem., Int. Ed.*, 2012, **51**, 12124–12127.
48 B. You, L. L. Wang, L. Yao and J. Yang, *Chem. Commun.*, 2013, **49**, 5016–5018.
49 Z. Y. Lin, M. K. Song, Y. Ding, Y. Liu, M. L. Liu and C. P. Wong, *Phys. Chem. Chem. Phys.*, 2012, **14**, 3381–3387.
50 Z. Y. Lin, G. Waller, Y. Liu, M. L. Liu and C. P. Wong, *Adv. Energy Mater.*, 2012, **2**, 884–888.
51 Z. Y. Lin, G. H. Waller, Y. Liu, M. L. Liu and C. P. Wong, *Carbon*, 2013, **53**, 130–136.
52 C. Zhang, T. X. Liu and X. H. Lu, *Polymer*, 2010, **51**, 3715–3721.
53 C. Zhang, L. L. Ren, X. Y. Wang and T. X. Liu, *J. Phys. Chem. C*, 2010, **114**, 11435–11440.
54 C. Zhang, W. W. Tjiu and T. X. Liu, *Polym. Chem.*, 2013, **4**, 5785–5792.
55 W. S. Hummers and R. E. Offman, *J. Am. Chem. Soc.*, 1958, **80**, 1339.
56 D. Hulicova-Jurcakova, M. Kodama, S. Shiraishi, H. Hatori, Z. H. Zhu and G. Q. Lu, *Adv. Funct. Mater.*, 2009, **19**, 1800–1809.
57 D. Zhou and B. Han, *Adv. Funct. Mater.*, 2010, **20**, 2717–2722.
58 M. M. Yang, B. Cheng, H. H. Song and X. H. Chen, *Electrochim. Acta*, 2010, **55**, 7021–7027.
59 S. Wang, L. Zhang, Z. Xia, A. Roy, D. W. Chang, J. Baek and L. Dai, *Angew. Chem., Int. Ed.*, 2012, **51**, 4209–4212.
60 Y. Wang, Y. P. Wu, Y. Huang, F. Zhang, X. Yang, Y. F. Ma and Y. S. Chen, *J. Phys. Chem. C*, 2011, **115**, 23192–23197.
61 Z. J. Fan, J. Yan, L. J. Zhi, Q. Zhang, T. Wei, J. Feng, M. L. Zhang, W. Z. Qian and F. Wei, *Adv. Mater.*, 2010, **22**, 3723.

